Viewing stomata in action: Autonomous *in planta* imaging of individual stomatal movement links morphology and kinetics

T. E. van den Berg, R. G. P. Sanders, E. Kaiser and J. Schmitz

Summary

Stomata regulate plant gas exchange with the environment, balancing between water loss and CO_2 uptake. Gas exchange dynamics are influenced by traits such as stomatal morphology, size and density, which are commonly investigated using imprints and manual microscopy, methods that are destructive and time consuming. Moreover, these microscopic properties are statically sampled and related to the dynamic ensemble behavior: gas exchange of an entire plant or part of a leaf. Knowledge on how morphology, size and density of stomata influence the movement of individual stomata is limited. We developed a compact microscope system that can measure the kinetics of tens of stomata *in vivo* simultaneously, with sub-minute time resolution. The system can be deployed in the plant's growth environment, at minimal impact on leaf microclimate. The characteristics of our microscope and data analyses are described, and we demonstrate its capabilities on *Chrysanthemum morifolium* with novel insight into individual stomata's contribution to water-use efficiency.

Introduction

Due to climate-change driven rises in temperature and Vapor Pressure Deficit (VPD) (Novick *et al.*, 2016) and decreased rainfall in many agricultural areas (Dore, 2005), future crop yields are coming under pressure. Adaptation of agriculture is therefore essential to maintain food security for an increasing world population (Anderson *et al.*,

2020). A pillar for agricultural adaptation is the development of varieties with increased water-use efficiency (WUE). To achieve this, we need to thoroughly understand the role that stomata play in plant WUE, defined as the rate of photosynthesis divided by the rate of transpiration (Bertolino *et al.*, 2019; Buckley, 2019; Lawson & Vialet-Chabrand, 2019; Nadal & Flexas, 2019), to breed for stomatal traits underlying high WUE.

Stomata are the microscopic pores on plant leaves that regulate their gas exchange, by dynamically opening and closing in response to environmental and intrinsic stimuli (Lawson & Matthews, 2020). Their dynamic behavior (Lawson & Vialet-Chabrand, 2019), morphology and density (Bertolino *et al.*, 2019; Duursma *et al.*, 2019) are important for plant WUE. Stomatal conductance to CO_2 diffusion into the leaf facilitates photosynthetic CO_2 fixation in the mesophyll, and stomatal movement broadly aims to balance the CO_2 taken up by photosynthesis with the water vapor lost through transpiration. Light intensity changes of ~25-50 fold on single leaves are frequent in the crop growth environment (Kaiser *et al.*, 2018). When the light intensity drops, the photosynthetic demand for CO_2 decreases near-instantaneously, while stomatal closure proceeds much more slowly. Hence, stomata that at that moment are open more than strictly necessary for CO_2 demand, waste water through unnecessary transpiration. Likely, fast-closing stomata are thus more water use efficient.

Stomatal clustering and density have major effects on WUE. The tendency to form clusters of stomata, compared to evenly spaced out stomata, negatively affects their function (and thereby WUE), by decreasing their effective response speed (Lehmann & Or, 2015). Higher stomatal density negatively impacts WUE, by increasing stomatal conductance under dark conditions, because stomata are often not fully closed (Duursma *et al.*, 2019). However, high stomatal density may increase stomatal speed and thereby WUE in fluctuating light, as it tends to correlate with small stomatal size (Bertolino *et al.*,

2019; Lawson & Matthews, 2020), indicating the complexity of stomatal trait effects on WUE.

An increase in light intensity quickly causes photosynthetic demand for CO_2 to increase, as biochemical limitations are lifted in the first minutes of photosynthetic induction (Sakoda *et al.*, 2021). To meet this demand for CO_2, stomata need to open to increase the rate of diffusion of CO_2, leading to a transient limitation of photosynthesis while opening. Transient limitations of photosynthesis in shade-sun transitions cost an estimated 10-40% of potential crop CO_2 assimilation (Long *et al.*, 2022). More efficient, fast-responding stomata could thus result in a CO_2 assimilation increase (McAusland *et al.*, 2016; Xiong *et al.*, 2018, 2022; Deans *et al.*, 2019; Acevedo-Siaca *et al.*, 2020, 2021; De Souza *et al.*, 2020; Taylor *et al.*, 2020; Eyland *et al.*, 2021), leading to similar potential increases in crop yield (Garcia *et al.*, 2023).

Stomatal dynamics are most frequently studied using leaf-level gas exchange measurements, and are then related to static microscopic observations of e.g. leaf epidermal peels to stomatal density and morphology. Measurements of bulk stomatal behavior, such as those of leaf gas exchange, hide the variation in dynamics between individual stomata (Kaiser & Paoletti, 2014), and studies that have resolved individual stomatal dynamics are relatively rare (Kaiser & Kappen, 1997, 2000, 2001; Kaiser, 2009; Grantz *et al.*, 2018). Moreover, minimizing the boundary layer of still air surrounding the leaf, as is common in gas exchange measurements (Busch *et al.*, 2024), limits the study of stomatal behavior under frequently occurring natural conditions, when a significant boundary layer is present. Therefore, information is lacking on how local morphology and density influence the ensemble of individual stomatal dynamics. Such characteristics could lead to a better understanding of stomatal control and thereby to breeding targets for WUE and yield (Haworth *et al.*, 2021). Additionally, it is essential to study such characteristics in the field, e.g. to understand how plants with altered stomatal

characteristics respond to multiple stresses in different developmental phases (Bertolino *et al.*, 2019).

Here, we describe a newly developed portable microscope, which can measure the opening and closure of tens of individual stomata simultaneously in the growth environment. Our method innovates on previous methods by selective use of green light for imaging and blue and red light as actinic light. In addition, we imaged the entire field of view (FOV) of the leaf's surface. We did this by creating large image stacks that were used to create leaf surface projections, in contrast to autofocus of single pores. This enabled us to relate stomatal dynamics to microscopic characteristics of the stomatal environment on the epidermis such as the distance to other stomata. Acquisition and analyses were largely automated, facilitating easy measurements. We demonstrated our method on leaves of *Chrysanthemum morifolium,* a greenhouse crop whose stomatal behavior can limit vase life (Fanourakis *et al.*, 2021) and the rate of photosynthetic induction (Zhang *et al.*, 2022).

Materials and Methods

Microscope

The design of our microscope focused on obtaining images with sub-micrometer resolution at different focus planes to resolve the 3D surface of the leaf with sub-minute time resolution. Additionally, the design aimed to be minimally invasive to the leaf's microclimate.

We achieved high optical resolution with high quality optics (plan APO series objectives, Mitutoyo, Japan and TTL200-S8 tube lens, Thorlabs, United States), verified with a calibration target (micro V2, Opto, Germany). The 20x objective (NA 0.42) enabled imaging of ~0.45 mm^2 (722x625 µm) of the leaf's surface. High time resolution of stacks of 100 images spaced 1 µm apart on the axis parallel to the imaging plane (z-axis; below the 1.6 µm depth of focus of the microscope objective) was achieved with a fast and accurate step motor (Z812, Thorlabs, United States, range of 12 mm, 0.2 µm

129 precision), which was controlled with autofocus software and a CMOS
130 camera (BFS-U3-244S8M-C; Teledyne-FLIR, Wilsonville, OR, USA). The
131 high sensitivity of the camera and on-camera pixel binning (2x2)
132 allowed us to achieve good quality images at a relatively low light
133 intensity (50 ± 10 µmol photons m^{-2} s^{-1}) and integration time (400 ±
134 100 ms). The use of long working distance objectives (20 mm) and leaf
135 clips that were laser-cut from transparent polycarbonate with 2 mm
136 neoprene cushions allowed us to clamp and image the leaf with low
137 obstruction to air flow and light. Imaging was strictly done with green
138 light (Effiring 525 nm; Effilux, Hürth-Efferen, Germany) in darkfield by
139 filtering light that passed through the objective with a bandpass filter
140 (FB550-40, 550 ± 8 nm, FWHM 40 ± 8 nm; Thorlabs, Newton, NJ, USA).
141 Monochromatic light was chosen, because it boosted image quality
142 by limiting chromatic aberrations. Green light was selected because
143 of its high reflectance and transmission by the leaf, higher optical
144 resolution achievable compared to near-infrared and a maximum
145 sensitivity of the camera in the green waveband. Optimization of
146 imaging light was achieved before each automated measurement by
147 manually changing the emission angle and diffusivity (by changing the
148 opacity of the window) of the imaging light. Blue-red actinic
149 illumination was emitted by a LED lamp (444/661 nm, 20/12 nm
150 FWHM, 52/48%; Seven steps to heaven, the Netherlands). Both
151 actinic and imaging light were controlled via LabVIEW (2018, National
152 Instruments, Austin, TX, USA) and intensity calibrated at the leaf
153 position with a PAR quantum sensor (Li-190R; Li-Cor Biosciences,
154 Lincoln, NE, USA). Leaves were clamped in the microscope leaf holder
155 equipped with embedded magnets at four contact points. The
156 portable microscope was mounted on a tripod and therefore
157 adjustable in height and angle to target leaves in a plant canopy (Fig.
158 1). Leaf Temperature and PAR intensity fluctuations during the
159 measurement were recorded with a leaf clip holder (2020-B)
160 connected to a portable fluorometer (MIN-PAM; Walz, Effeltrich,
161 Germany).

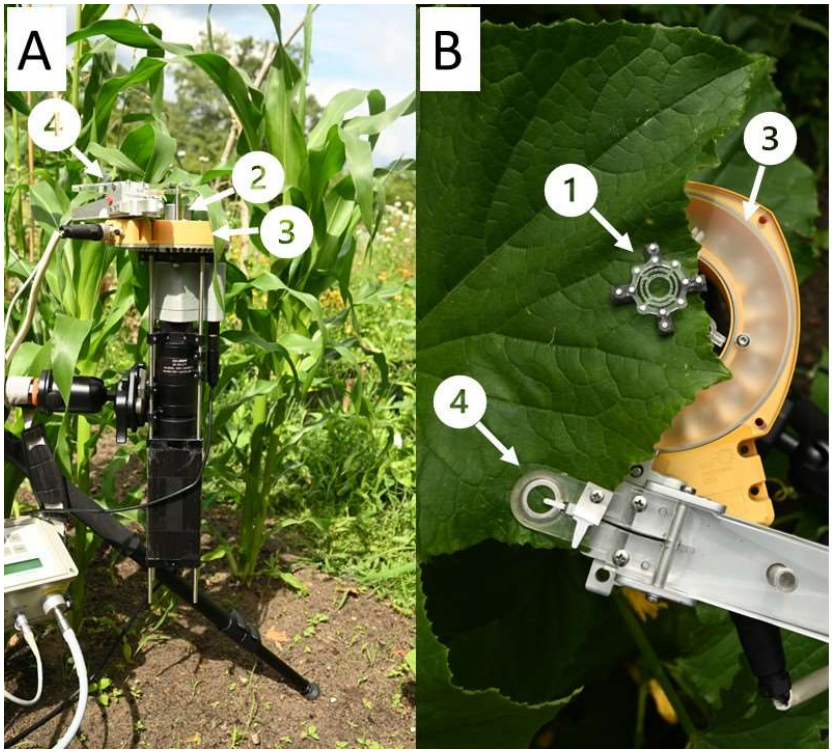

Figure 1. Example of the microscope in use at the vegetable garden of the University of Twente (the Netherlands). A. Side view of the entire microscope with a leaf of Zea mays clamped in the holder. B. Top view of a leaf of Cucumis sativa clamped in the holder. The leaf clip (1) holds the leaf in place via magnets embedded in the polycarbonate framework. Neoprene cushions ensure a minimal effect of the clamping on the surface of the leaf. The microscope objective (2) can focus automatically and the ring light (3) provides illumination for microscopy. The leaf clip from the mini-PAM (4) records fluctuations in PAR as well as ambient air temperature (A) or leaf temperature (B).

Software

Acquisition

The data acquisition software was developed in Labview. Camera settings, number of images per stack with different focus planes on the z-axis (z-stack) and stack depth, imaging and stimulus light intensity and duration, as well as autofocus settings that determined the position of the stack's center (methods: Roberts, Sobel, Gradient (Lthi *et al.*, 2010)) were controlled via Labview's user interface. Full protocol files with imaging, light timing as well as light intensity settings can be loaded into the software with a graphical user interface for inspection.

Analyses

Acquired z-stack images, in 16bit TIFF format belonging to each z-stack, were processed in several stages (Fig. 2) using Fiji open-source

software (Schindelin et al., 2012). Images were denoised (despeckle and outlier removal), normalized for intensity (enhance contrast, normalize) and aligned (SIFT linear stack alignment (Lowe, 2004)). SM movie 1 is an example of a processed image stack. Next, the plugin "extended depth of field" (Forster *et al.*, 2004) was used to generate a focus projection of the leaf surface, reducing the stack to a single image per timepoint. All timepoint focus projections were then stacked again to generate a video of the entire experiment that was again aligned to adjust for x-y axis movements of the leaf during the experiment (SIFT linear stack alignment). This stack was then cropped, to include only the area that was within view during the entire experiment, shadow corrected with the pseudo flat field correction in the BioVoxxel plugin (Brocher, 2015) and contrast enhanced using the CLAHE algorithm (Reza, 2004) (Fig. 3 A-C). SM movie 2 is an example of a processed video from an entire experiment, while SM movie 3 is a zoomed version of a single stoma. Auto thresholding was done in Percentile mode (Doyle, 1962), as it generated the best segmentation of open pores for *Chrysanthemum morifolium* (Fig. 3D). SM movie 4 is the same video as SM movie 3 after thresholding. Stomata in the stack were manually selected with the elliptical selection tool and added in the region of interest (ROI) manager (ImageJ). Pore areas were then quantified via the 'analyse particles' menu for each stoma in the ROI manager, to quantify pore area and to generate masks for visual inspection of pore shapes for the entire experiment (Fig 3D). SM video 5 shows the masks generated from the stoma in SM videos 3 and 4.

Kinetics of stomatal aperture changes were loaded into Origin (OriginLab Corporation, Nothampton, MA, USA) and, data of opening and closing were fitted separately with the model (Vialet-Chabrand *et al.*, 2013):

Equation 1

$$A(t) = (A_{max-i} - A_{0-i})\, e^{-e^{\left(\frac{\lambda_i - t}{k_i} - 1\right)}} + A_{0-i}.$$

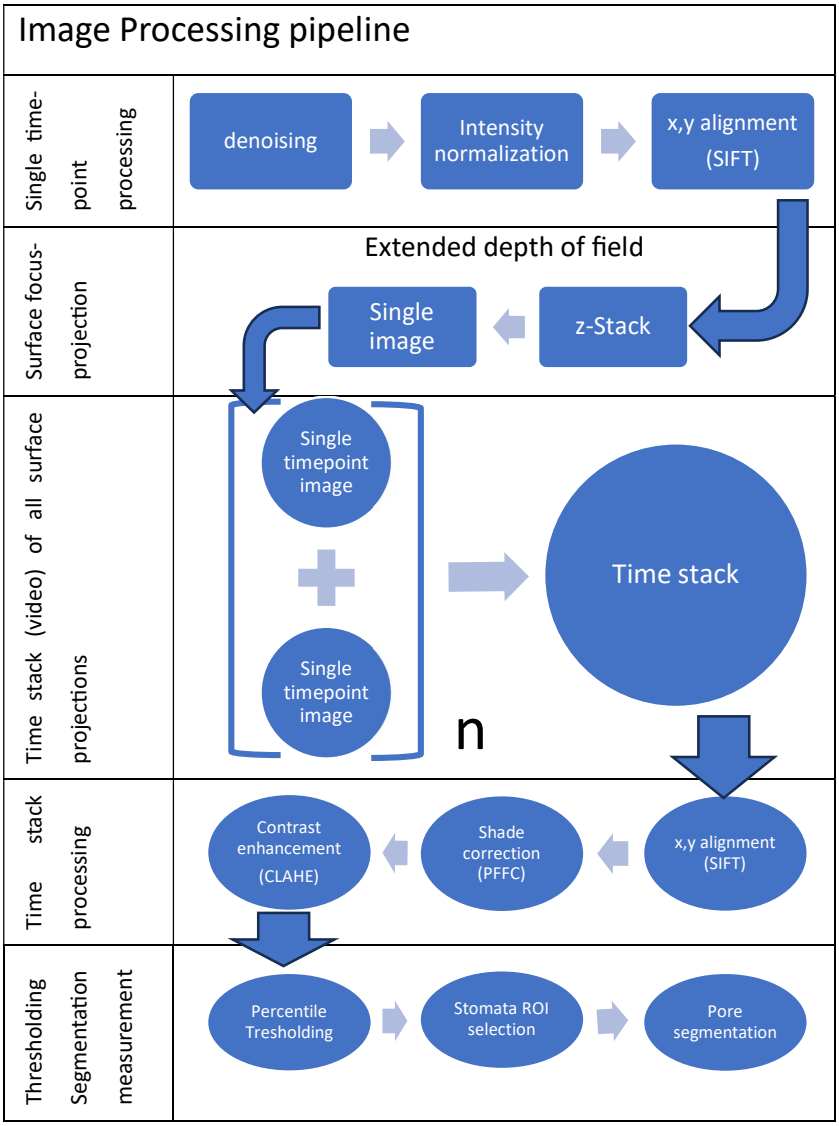

Figure 2. Flow chart of image processing pipeline. Single images belonging to an image stack were denoised and their contrast was enhanced by intensity normalization. Images with different z-axis position in a stack were then aligned to correct for minor x, y movements (surface parallel to the microscope's objective). The extended depth of field plugin processed the stack to create a single focus projection of leaf surface. Each surface projection timepoint was added together in a video of the entire experiment. The images in these videos were again aligned to correct for x, y movements, shade corrected and their contrast was enhanced. Automated thresholding of time stacks was done with Percentile mode. Stomatal positions were manually selected with the elliptical selection tool, pore area was segmented, and quantified with the analyze particles menu.

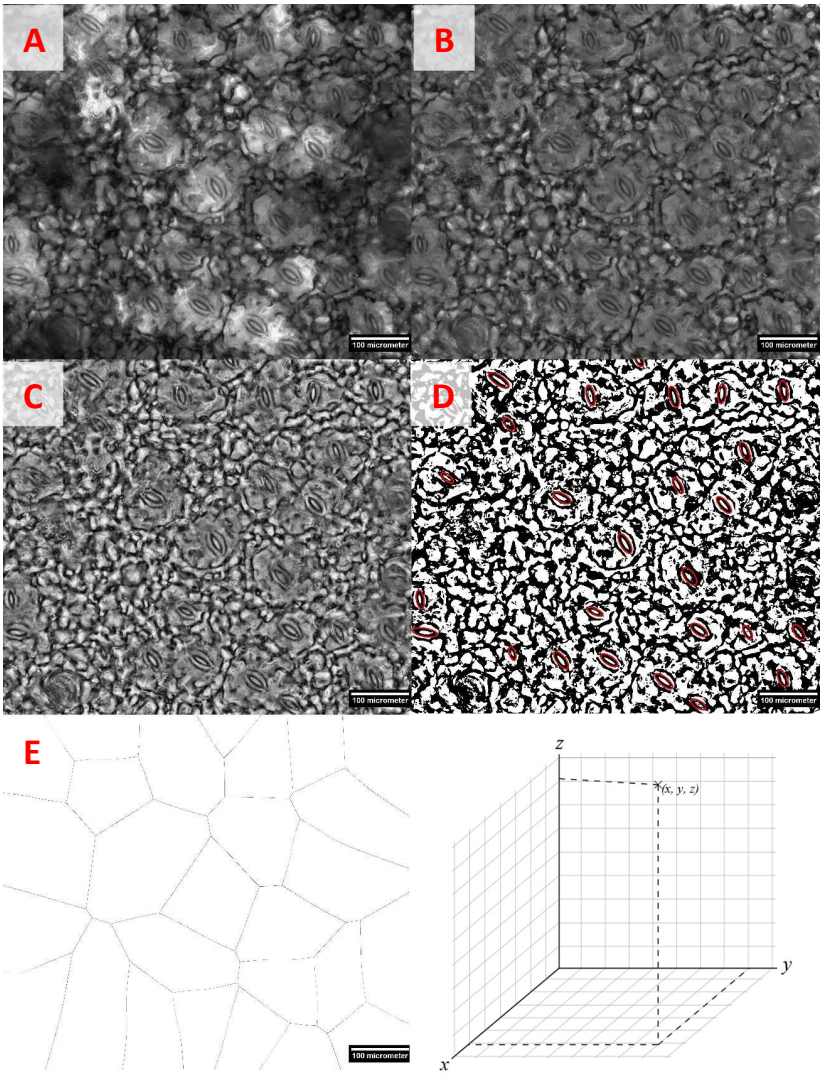

Figure 3. Example of time-stack processing with a single surface projection. A. Surface projection output from extended depth of field. B. Image in A processed with pseudo flat field correction (PFFC). C. Image in B processed with contrast limited adaptive histogram equalization (CLAHE). D. Image in C after thresholding with the Percentile method. Red ROIs are drawn manually with the elliptical selection tool. E Voronoi diagram drawn based on the elliptical selections of stomata in D. The scale bar indicates 100 micrometer.

With A(t) the stomatal aperture at time t, A_{max} the maximum aperture at steady-state, A_i the initial aperture at steady-state, λ the time lag of the response (min) and k the time constant (min), a measure of the rapidity of the response. For stomatal closure, $A_{min\text{-}d}$ was defined as the final aperture at steady-state with $A_{0\text{-}d}$, the aperture at the start of the closing response. k and λ were separately quantified for open and closing responses, using subscripts i and d, respectively.

Equation 2

$$A(t) = (A_{min-d} - A_{0-d})\, e^{-e^{\left(\frac{\lambda_d - t}{k_d} - 1\right)}} + A_{0-d}.$$

Quality of fit was assessed by reduced chi squared statistic of the fit (ideally close to 1), the structure in the residuals (ideally random noise without structure) and error estimates of the fitted parameters (ideally <10%, but no larger than 100%). SM Fig. 1 provides an example of fit of the kinetics for a single stoma.

Some stomata were excluded from data analysis. Reasons to exclude stomata were: a) Bad segmentation due to low local image quality e.g. stoma shaded by trichome, b) incomplete stomatal pore on the edge of an image, c) lack of pore opening after a light intensity change, d) low-quality fit, as judged by χ^2, residuals and uncertainty (>100% of value) in the fitted parameters.

Guard cell length (GCL) was measured in Fiji by manual use of the straight line tool in the image at t=90 min, the timepoint where stomatal aperture was generally maximal.

A Voronoi plot (Fig. 3E), which connects lines with equal distance to the borders of each neighbouring stoma, was created via the Voronoi tool (in the Fiji software), and each surface was measured via the 'analyse particles' menu. Resulting data were used to test for relationships between the leaf area that could be assigned to a given stoma ('Voronoi area') and that stoma's aperture and kinetics. Only Voronoi surface areas that were fully inside the image were considered in this analysis.

Because our method depends on the automated focus projection of the z-stack (the reduction into a single image that represents the entire surface within the FOV), we compared it to the human operator: manual selection of the best focus position per pore. We compared the results for ten stomata with a good distribution within the FOV for 100 stacked images per 119 time points during the long term shade-sun-shade transition. Further image processing,

278 segmentation and quantification of the pore area were automated
279 and following the identical protocol for both manual selection and
280 focus projection.

281 Plant material and growing conditions

282 *Chrysanthemum*

283 Experiments were conducted in a growth chamber equipped with
284 nine dimmable LED modules (DRWFR_RSE 400V 1.1D MP; Signify,
285 Eindhoven, the Netherlands) that produced a diurnal average of ~250
286 μmol m^{-2} s^{-1} of photosynthetically active radiation (PAR) at plant
287 height. A sinusoidal light pattern (16h light period, minimum PAR of
288 120 μmol m^{-2} s^{-1}, maximum PAR of 1200 μmol m^{-2} s^{-1}) was applied with
289 random drops in light intensity that mimicked natural irradiance
290 fluctuations. The timing and extent of drops in light intensity changed
291 daily, but the sinusoidal pattern and daily light sum remained fixed.
292 Temperatures were set at 23/20 °C (day/night). Relative air humidity
293 was 70%. Ventilation was 0.28-0.55 m s^{-1} of laminar flow.
294 *Chrysanthemum morifulium* (cv. Anastasia; Deliflor Chrysanten,
295 Maasdijk, the Netherlands) plants that had been grown in plastic pots
296 (diameter 14 cm, filled in with potting soil) were cut back at the third
297 or fourth node to allow for the formation of new axillary buds. Plants
298 were irrigated twice per day (at 7:00 and 19:00 h) with nutrient
299 solution, using an automatic ebb and flow system.

300 Stomatal aperture measurements

301 Stomatal apertures were measured on fully expanded leaves in the
302 middle between the leaf edge and the midrib. Care was taken not to
303 include veins in the FOV of the microscope, in order to maximize the
304 number of stomata in the FOV. A screen was used to shade the
305 measured plant from direct growth chamber lighting during aperture
306 measurements. Leaves were acclimated to 50 µmol m^{-2} s^{-1} blue-red
307 light and 50 µmol m^{-2} s^{-1} green imaging light for 60 minutes before
308 image acquisition was started. Image stacks were acquired every
309 minute for 120 minutes. After 30 minutes, the light intensity was
310 increased to 1000 µmol m^{-2} s^{-1} by increase of the blue-red light

intensity to 950 µmol m^{-2} s^{-1}. After 60 minutes, the blue-red light intensity was switched back to 50 µmol m^{-2} s^{-1} (total intensity including green measuring light: 100 µmol m^{-2} s^{-1}) for 30 minutes to trigger stomatal closure.

Statistical Tests

All statistical tests were performed in Origin (OriginLab). Normality tests for the distribution of fit or measured parameters were performed with Shapiro-Wilkins test. KWANOVA and paired Wilcoxon signed rank tests were used to test for significant differences between sets of parameters that were not normally distributed. Spearman's correlation was calculated between set of parameters that were not normally distributed. For normally distributed data, students t-test and Pearson correlations were used. The number of replicates and the probability scores are mentioned with the test results.

Results

Our portable microscope enabled the imaging of stomatal dynamics of *Chrysanthemum* in the growth environment by its selective use of green light, with limited effects on stomatal movement (Jones *et al.*, 2022) for imaging at a low light intensity, while using stepwise changes in red and blue light intensity to trigger changes in stomatal aperture.

Comparison of stomatal pore area dynamics between automatic and manual selection of best focus per pore

The dynamics of the pore area in the focus projection images (automatic) were generally well correlated with those in the manually selected best single focus images (Fig. 4A, SM Fig. 2, table 1). However, the pore area tended to be smaller when derived automatically: pores were on average 10 μm^2 smaller in automatic than in manual images, with slightly larger differences during the first 45 min of the experiment (Fig. 4B). To investigate if this difference in pore area arose from spatial dependence of image quality, we correlated the difference against positional coordinates of the stomata. We found that these differences between automatic and

manual-derived pore area were neither correlated to the x, y position of the pore in the image, nor to the distance of the pore to the image edge, nor to the position in the stack of the manual images (Table 2). Further, pore opening in the automatic images tended to be faster than in the manual images, as indicated by the k_i parameter of the model (Table 1), although this difference was not significant. Pore closing speed was similar in both image sequences. In conclusion, the automatic method can correctly asses the kinetic parameters of the stomata but underestimates the true pore area.

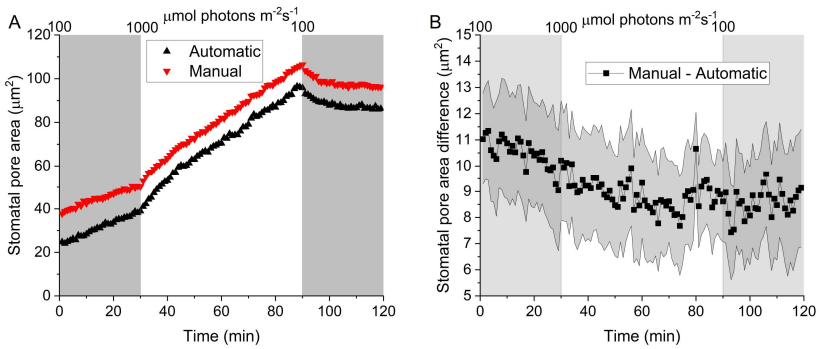

Figure 4. A Example of kinetics of one stoma analyzed with the focus projection (automatic) method or in the manually selected best single focus images (manual) demonstrating their correlation. All individual stomata curve pairs are in SM Fig 2. B Averaged difference in pore area between the same pore analyzed in the automatic images and the Manual images in all timepoints of the shade-sun-shade transition. The shaded area around the curve indicates the standard error of means. Light grey blocks indicate shade periods.

Table 1. Averaged fit parameters of the kinetic model for the pore areas in the automatic and manual images as well as Pearsons correlation coefficient between the pore area kinetics in automatic and manual images. NS indicates no significant differences between the means as tested with a paired T-test (for k_i and k_d) or non-significant correlation (P>0.05). k_i and k_d were normally distributed (Shapiro-Wilkins test). Errors indicate the SEM.

Method (n=10)	k_i (min) NS	k_d (min) NS	Pearsons r	
			automatic	manual
automatic	30 ± 2	2.8 ± 0.4	1	>0.97 (P<0.0001)
manual	36 ± 3	3 ± 1	>0.97 (P<0.0001)	1

Table 2 Pearsons or Spearmans correlation coefficient between the average automatic-manual difference and the x, y and z coordinate of the pore and the distance to the image edge. Distance to image edge was not normally distributed in contrast to the coordinates or the z-position in the stack (Shapiro-Wilkins test)

therefore Spearman correlation is used. NS indicates non-significant correlation (P>0.05).

Pearsons r or Spearmans ρ	X coordinate (r)	Y coordinate (r)	Distance to image edge (ρ)	z-position in stack (r)
manual-automatic	-0.16 (NS)	0.20 (NS)	0.24 (NS)	-0.36 (NS)

Movement of the leaf surface upon light intensity change

Because we recorded the changes in the position of the leaf surface via automatic adjustments by the step motor of the microscope, we could observe the movement of the leaf surface upon changes in light intensity (Fig. 3C). Specifically, after the switch from 100 to 1000 µmol m^{-2} s^{-1}, there appeared to be some shrinkage or bending of the leaf as its surface moved away from the camera, whereas upon the transition from 1000 to 100 µmol m^{-2} s^{-1}, the opposite happened (Fig. 5). These leaf surface movements had no impact on imaging, because the FOV of the leaf was always captured in focus within the stack. Leaf surface movements resulted in a minor displacement of the position of the leaf surface in the stack (SM Fig. 3). In conclusion, the active repositioning of z-positions of each new image stack based on the z-position of the leaf surface in the previous image stack, is necessary because the leaf surface moves hundreds of micrometers during light intensity changes.

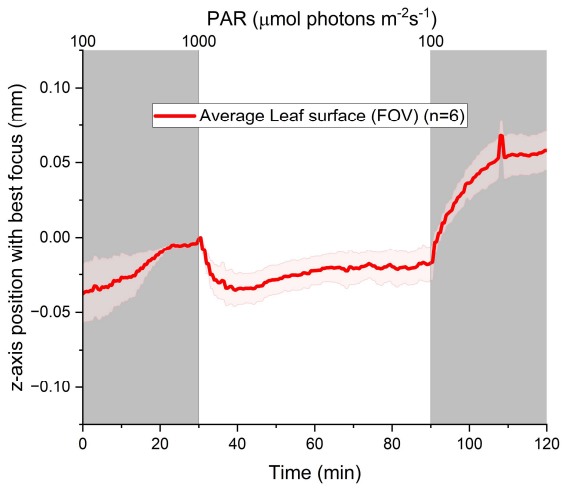

Figure 5. Position on the z-axis of the imaged area of the leaf surface where the largest area of leaf surface was in focus during the shade-sun-shade experiment. The red curve indicates the average of six biological replicates, and the shaded area indicates the standard error of the mean. The z-axis position at t=30 min was set to zero for each measurement before averaging. The Focus position (y-axis) indicates the middle position of the 100 images per one minute timepoint that were spaced 1 µm apart.

Stomatal dynamics of Chrysanthemum leaves during a shade-sun-shade transition.

To further demonstrate the power of our method, we continued to test the resolving power of the method in leaves of six plants split over two cultivation periods. After image processing, ~78% (124/158) of the stomata in the FOV were kinetically resolved (Fig. 6).

While overall stomatal aperture was in a steady-state in the initial shade condition (Figure 6, 0-30 min), individual stomata showed minor movements by either opening or closing only slightly. After the light intensity was increased, 62% of stomata (77) immediately opened their pores, while the rest showed a lag in their response of up to 40 min (Fig. 6). A duration of 60 min at 1000 µmol photons m^{-2} s^{-1} was not sufficient to reach a steady-state pore opening for most stomata, which led to more uncertainty in the fitted k_i parameter than if a steady-state had been reached. Figure 7 and 8 show the distribution of the fitted parameters in violin plots.

The light intensity decrease led to an immediate closing response of thirteen stomata (13%), with the rest lagging in their response. Nineteen stomata did not close at all within the 30 min sun-shade transition (20%). These 19 stomata had a significantly higher steady-state aperture under high light intensity than the 78 stomata that closed during the shade phase ($A_{max\text{-}I}$ 78±6>60±3, mean+SE, P<0.02, KWANOVA). In addition, they were not evenly distributed among the biological replicates: of the 19 non-closing stomata, 15 were located on one biological replicate and the remaining four stomata from two others (1 and 3 per replicate), while the remaining replicates had none. A steady-state was reached for all but five of the stomata that closed within the 30 min sun-shade transition, however this new steady-state pore aperture at lower light intensity was larger

than the initial steady-state level of these stomata before the opening light stimulus was applied ($A_{min\text{-}d}$ 23±3 µm^2 > $A_{0\text{-}i}$ 13±2 µm^2, mean+SE, paired sample Wilcoxon Signed Ranks Test, P<0.005).

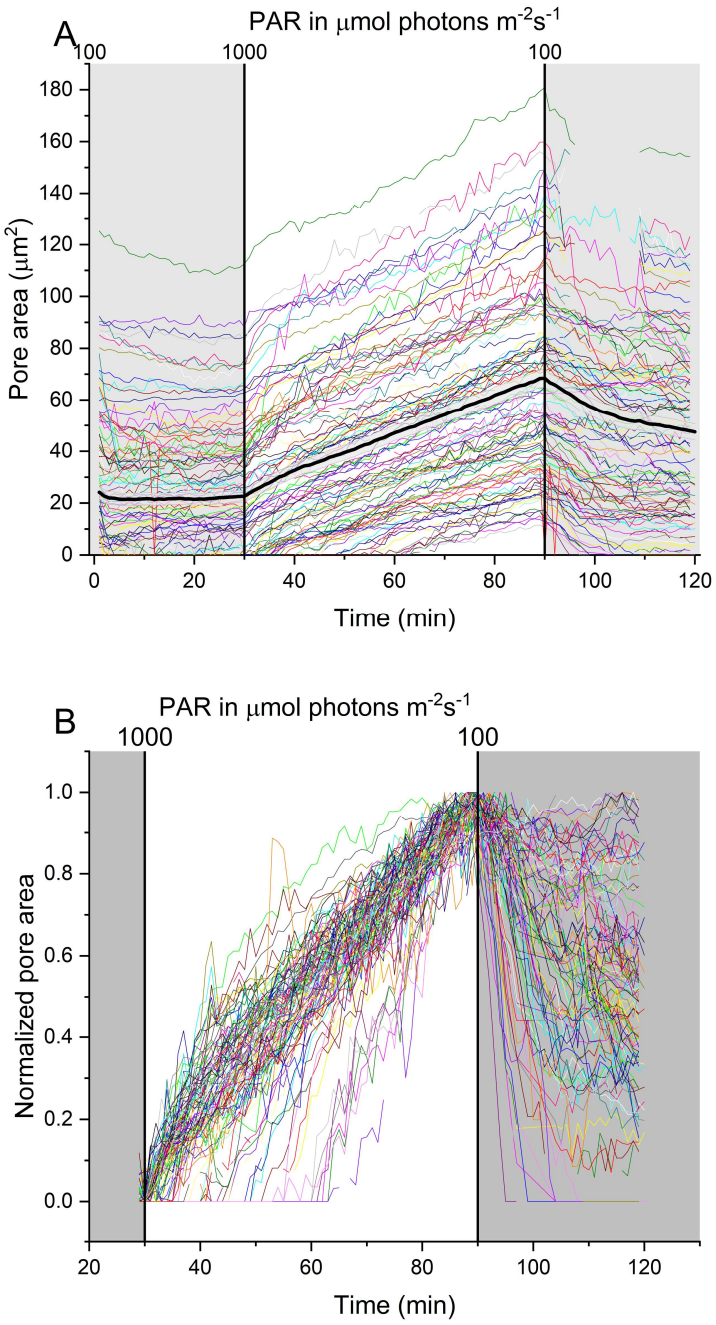

Figure 6. A Example of stomatal pore area changes upon a shade-sun-shade transition. Single lines show values of 124 individual stomatal pores from six chrysanthemum plants. The thick black curve represents the average, and the grey area the standard error of the mean. During the second shade period, a temporary loss of focus during one measurement caused fewer data points to be recorded. B Kinetics of all stomata shown in A, normalized to 0 at t=29 min just before the light intensity was increased and to 1 for the maximum aperture reached at 1000 µmol photons m^{-2}s^{-1}, highlighting the differences in opening lag (λ_i) and stomatal closure.

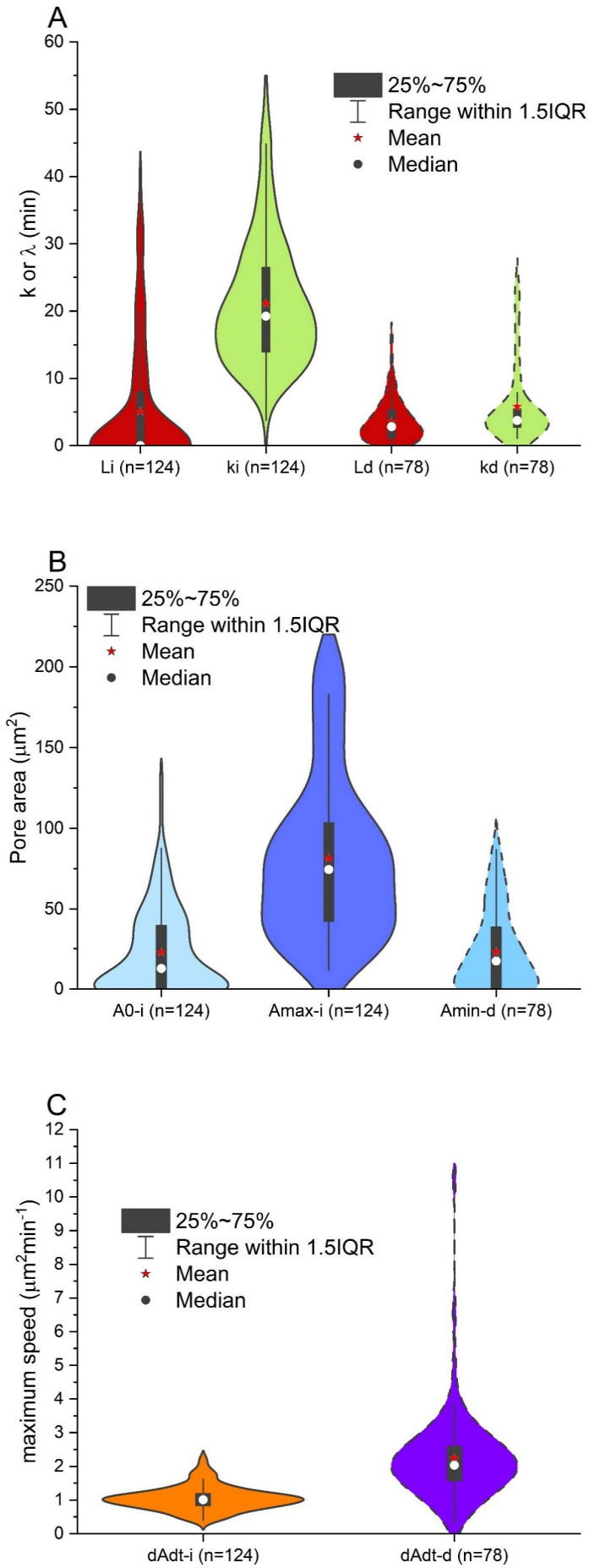
A
k or λ (min)
25%~75%
Range within 1.5IQR
Mean
Median
Li (n=124)
ki (n=124)
Ld (n=78)
kd (n=78)
B
Pore area (μm²)
A0-i (n=124)
Amax-i (n=124)
Amin-d (n=78)
C
maximum speed (μm²min⁻¹)
dAdt-i (n=124)
dAdt-d (n=78)

440

Figure 7. Distributions of parameters obtained from model fits to stomatal kinetics (raw data shown in Fig. 6). A. Opening and closing lag (Li, Ld) as well as time constants for opening and closing (ki, kd) B. Steady-state stomatal pore area in the initial shade period A_0, in sun period A_{max-I} and the final shade period A_{min-d}. C Maximum opening $dAdt_i$ and maximum closing speed $dAdt_{.}$ Red stars represent the mean and circles the median of the data, 25-75% indicates the position were the middle 50% of the values in the distribution can be found and the range within 1.5 IQR indicates which part of the distribution are not considered to be outliers.

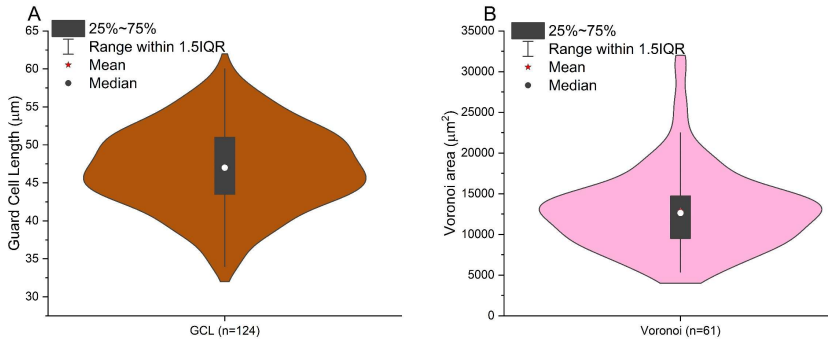

Figure 8 Distribution of A. guard cell length (GCL) of the stomata in Fig. 6 measured in the last image during the high light period (t=89 min) and B. Voronoi area representing the area on the leaf that is within the shortest distance to a given stoma. Red stars represent the mean and circles the median of the data, 25-75% indicates the position were the middle 50% of the values in the distribution can be found and the range within 1.5 IQR indicates which part of the distribution are not considered to be outliers.

Of the 78 stomata that opened and closed, only six had a larger k_i than k_d and those k_d were the very highest among the 78 values (Fig. 7A), meaning that for the majority of stomata, the steady-state when closing was reached faster than when opening.

Of all parameters, only guard cell length was normally distributed (Shapiro Wilkins test, $p<0.001$), therefore Spearman's nonparametric ρ was used to investigate correlations. A higher aperture during the first shade phase (A_{0-i}) was strongly correlated with a higher maximum aperture in the sun phase (Figure , A_{max-i}, $\rho=0.89$, $p<0.001$) and moderately correlated to the steady-state aperture during the second shade phase (A_{min-d}, $\rho=0.55$, $p<0.001$). A_{max-i} was also moderately correlated to k_i ($\rho=0.63$, $p<0.001$) and $dAdt_{max-i}$ open ($\rho=0.54$, $p<0.001$). The time-lag of the opening response (λ_i) was negatively correlated to A_{0-I}, A_{max-I}, $k_{i,}$ GCL, Voronoi A_{min-d}, k_d and $\lambda_{d,}$ and positively correlated to the closing speed $dAdt_{max-d}$. Interestingly, the time-lag of the closing response (λ_d) was correlated to A_0 ($\rho=0.54$, $p<0.001$) and A_{max-i} ($\rho=0.54$, $p<0.001$).

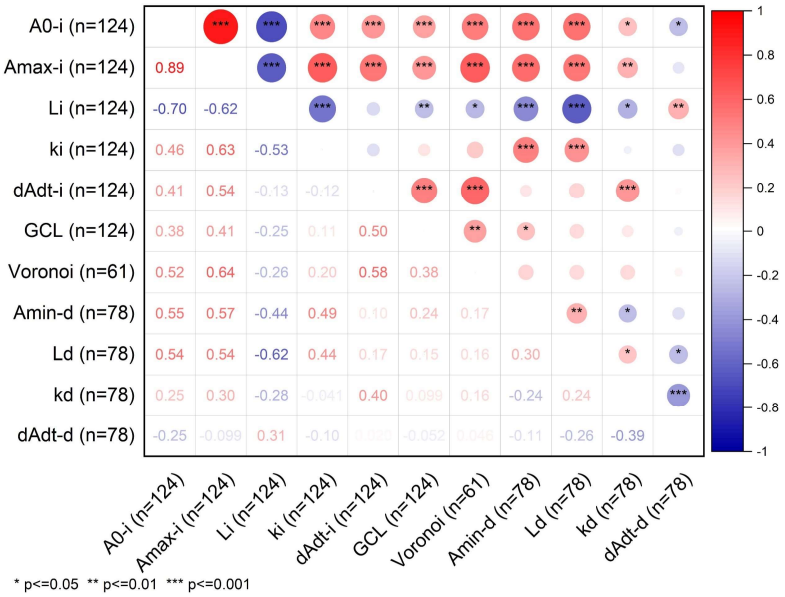

Figure 9. Spearman's correlation matrix between parameters of individual Chrysanthemum stomata (based on Fig. 7 and 8). A_0, fitted steady-state aperture under 100 µmol photons $m^{-2}s^{-1}$ PPFD. A_{max}, predicted steady-state aperture under 1000 µmol photons $m^{-2}s^{-1}$ PPFD; k_i, time constant for apertures to increase to A_{max} under 1000 µmol photons $m^{-2}s^{-1}$ PPFD; k_d, decrease from A_{max} to A_f under 100 µmol photons $m^{-2}s^{-1}$; l , initial lag in the response time of stomatal aperture to a step increase in PPFD; max dAdt, maximum rate of stomatal opening or closing to an increase or decrease in PPFD from 100 to 1000 µmol photons $m^{-2}s^{-1}$ or vice versa. Anatomical parameters of guard cell length (GCL) and width (GCW) were also compared. The Voronoi area represents the fraction of the leaf that is within the shortest distance to that stoma.

Among the anatomical parameters, Guard cell length (GCL) was moderately correlated to the maximum opening speed ($dAdt_{max-i}$, ρ=0.5, P<0.001), initial (A_{0-I}, ρ=0.38, P<0.001), maximum (A_{max-I}, ρ=0.41, P<0.001) and final aperture (A_{min-d}, ρ=0.24, P<0.05) as well as the Voronoi area (ρ=0.38, P<0.01). The Voronoi area was in addition moderately correlated with A_{0-i} (ρ=0.52, p<0.001), A_{max-i} (ρ=0.64, p<0.001) and the maximum opening speed ($dAdt_{max-i}$, ρ=0.58, P<0.001).

In conclusion, our method resolved 11 different kinetic and non-kinetic parameters for up to 78% of the stomata within the FOV to generate new insight into the WUE of individual stomata.

Discussion

The portable microscope presented here provides a new way to study the opening and closure of individual stomata in the growth

environment. This method facilitates analyses of individual stomatal dynamics in relation to their local morphology and anatomy.

Our hardware and method are distinct from several previous studies that imaged stomata *in situ* (Kaiser & Kappen, 1997, 2001; Kaiser, 2009; Grantz *et al.*, 2018). The main differences and their advantages and disadvantages are listed in Table 3.

Table 3 Differences between this work and prior studies (Kaiser & Kappen, 1997, 2001; Kaiser, 2009; Grantz et al., 2018) with their advantages and disadvantages

Difference	Advantage	Disadvantage	Study
525 nm versus 880 nm imaging light	Higher optical resolution	Imaging light is photosynthetically active	(Kaiser & Kappen, 1997, 2001)
Autofocus per stack instead of per pore	Imaging speed is not limited by number of stomata but only by stack size	Can cover stomata in only a small area of the leaf (~1 mm^2)	(Kaiser & Kappen, 1997, 2001; Kaiser, 2009; Grantz et al., 2018
Kinetic model fitting	Quantitative comparison of fit parameters	-	
No Gas exchange chamber	More natural boundary layer conditions	No information on leaf bulk gas exchange	(Kaiser & Kappen, 1997, 2001; Kaiser, 2009; Grantz et al., 2018

A major contrast with prior studies is that the way the leaf is clamped was minimally invasive to the leaf's microenvironment, with free transpiration on both sides of the leaf, because no gas exchange measurements were performed. The boundary layer was not regulated, reflecting a more natural condition. Another major difference was the sampling of stomata: prior studies have randomly

515 sampled stomata distributed over a large area (>1 cm^2), whereas we
516 resolved as many stomatal kinetics as possible within ~1 mm^2, to
517 relate their kinetic behavior to the local morphology on the surface of
518 the leaf. In doing so, we reached a higher time resolution of, on
519 average, 21 stomata min^{-1} compared to 75 stomata once every 6-7
520 min (Grantz *et al.*, 2018). Another major difference is that we fit a
521 kinetic model to individual stomatal aperture kinetics to investigate
522 the relation of model parameters to parameters related to the local
523 morphology on the leaf surface.

524 A clear limitation of our method is the underestimation of pore area
525 compared to manual selection of the best focus per pore (Fig. 3). This
526 is especially concerning for pores that only opened minimally, as
527 these were likely found to be closed even when they were not actually
528 closed. Such pores are scored with large opening lags that are
529 erroneous. The minimal resolvable pore area is effectively limited
530 beyond the optical resolution of the microscope to ~10 μm^2 for the
531 20x objective used here. This limitation of the automated focus
532 projection method is not absolute but scales with the numerical
533 aperture of the objective. Minimally resolvable pore area can thus still
534 be improved at the cost of FOV size and working distance. The
535 smaller pore area in the automated focus projection method is likely
536 due to differences in absolute contrast between the automatic and
537 the manual images that lead to different thresholding by the
538 percentile method. Implementation of the state-of-the art in
539 computer vision solutions, such as StomaAI (Sai *et al.*, 2023), for
540 stomatal measurements and segmentation may increase the
541 resolving power in the future.

542 The analysis of dozens of *Chrysanthemum* stomata led us to
543 the novel insight that a larger aperture at steady-state in high light
544 intensity ($A_{max\text{-}i}$) was positively correlated with the time lag for the
545 closing response (λ_d), with a large negative consequence for WUE
546 (Lawson & Blatt, 2014). Stomata with larger pores may suffer from a
547 larger lag in their response because of a stronger hysteresis.
548 Hysteresis is related to the opening speed at the time of the change

549 in light intensity, with opening speed ($dAdt_i$) positively correlated with
550 the maximum aperture (A_{maxi}).

551 Across a number of species, Deans *et al* (Deans *et al.*, 2019)
552 found that a large stomatal conductance at high light intensity was
553 correlated with fast closing response, to compensate in water-use
554 efficiency. We could not corroborate this for $A_{max\text{-}i}$ and their rate of
555 closing $dA/dt_{max\text{-}d}$ in individual stomata. *Chrysanthemum* stomata
556 with a large aperture thus have a disproportionately large negative
557 contribution on WUE normalized for their apertures, due to the
558 observed correlation between $A_{max\text{-}i}$ and the time lag for the closing
559 response λ_i, combined with a similar closing speed as stomata with a
560 smaller aperture.

561 Stomatal size was found to be negatively correlated with WUE
562 across different *Arabidopsis* ecotypes (Dittberner *et al.*, 2018). A high
563 WUE is typically associated with a fast rate of stomatal closure
564 (Lawson & Vialet-Chabrand, 2019), and smaller stomata have indeed
565 often been observed to open or close faster than larger stomata
566 (Drake *et al.*, 2013; Kardiman & Ræbild, 2018; Durand *et al.*, 2019). In
567 contrast, we found a strong positive correlation between GCL and
568 maximum opening speed, as observed before for elliptical/kidney-
569 shaped stomata (McAusland *et al.*, 2016). The relation between
570 stomatal size and speed may thus be more complex than previously
571 assumed. This relation could be species dependent, as no correlation
572 between stomatal size and speed was found in a diverse range of
573 plants with differing stomatal morphologies and physiological
574 behaviors (Haworth *et al.*, 2018). Additionally, it may depend on the
575 type of stimulus, since e.g. step changes in light intensity and in VPD
576 often trigger different dynamics (Durand *et al.*, 2019).

577 The opening and closing speeds of stomata, that were not
578 correlated here, were found to be positively correlated in some
579 studies (Haworth *et al.*, 2021), but showed no correlation in others
580 (Xiong *et al.*, 2018). The correlation between opening and closing
581 speed may thus be species and/or condition dependent.

582 Mesophyll airspace formation is linked to functional pores
583 (Lundgren *et al.*, 2019), therefore we assumed that there was a
584 mesophyll airspace under each functional pore. We further assumed
585 that the diffusion pathway to the surrounding mesophyll was
586 approximately equal in all directions and that the majority of CO_2
587 feeding the mesophyll directly underneath the leaf surface was
588 supplied by stomata on that surface and not by stomata on the
589 opposite side of the leaf. Finally, we assumed that airspace and
590 mesophyll were homogeneously distributed below the pores. The
591 positive correlation of A_0 and A_{max} with the Voronoi area of the stoma
592 can be interpreted as the stoma matching its aperture to the local
593 demand for CO_2 from the direct mesophyll below. If a stoma has to
594 supply a larger area of mesophyll, its steady-state aperture will be
595 larger under all light conditions than that of a stoma that supplies a
596 smaller area of mesophyll. The same reasoning can be applied to the
597 opening speed: if one stoma 'feeds' a large mesophyll area with CO_2,
598 drawdown of C_i during photosynthetic induction will likely be stronger
599 compared to a stoma that supplies a smaller area, and the signal for
600 fast stomatal opening may thus be stronger. An alternative
601 explanation for the positive correlation of A_0 and A_{max} with the
602 Voronoi area may be that a larger Voronoi area supplies the guard
603 cells with more solutes, water and space to open than a smaller
604 Voronoi area.

605 Conclusions

606 We showed here that *in vivo* microscopy of stomata in the leaf's
607 growth environment could be used to generate stomatal opening and
608 closure dynamics in dozens of neighboring individual stomata. Our
609 method, which uses green light for imaging and generates focus
610 projections of the entire leaf surface within the FOV, resolved the
611 kinetics of 78% of *Chrysanthemum* stomata, on average 21 stomata
612 min^{-1} during a shade-sun-shade transition. Pore area kinetics were
613 fitted with a model developed for stomatal conductance time courses
614 and show the substantial variation between individual stomata.
615 Correlation between the fitted parameters led us to discover that

pores with larger apertures in high light have a larger lag time in their closing response, and thereby contribute disproportionately to a lower WUE.

Acknowledgements

We thank Seven-steps-to-heaven for their in kind support of the actinic light source. We acknowledge 4TU HTSF Plantenna for financial support. Silvere Vialet-Chabrand and Ep Heuvelink are acknowledged for helpful discussion of the results.

Competing interests

None declared

Author contributions

Conceptualization T.B. and J. S., Hardware T.B. R.S. Software T.B., R.S., Growing facilities E.K., Experimentation T.B., Data Analyses T.B., Writing the first draft T.B., Critical review of the manuscript T.B., E.K., J.S., Funding J.S.

Data availability

All data is available upon request. For more information and software updates: GitHub - Plantenna/Stomata-microscope: Non-invasive microscopic imaging of individual stomatal kinetics in the growth environment with high resolution

References

Acevedo-Siaca LG, Coe R, Quick WP, Long SP. **2021**. Variation between rice accessions in photosynthetic induction in flag leaves and underlying mechanisms. *Journal of Experimental Botany* **72**: 1282–1294.

Acevedo-Siaca LG, Coe R, Wang Y, Kromdijk J, Quick WP, Long SP. **2020**. Variation in photosynthetic induction between rice accessions and its potential for improving productivity. *New Phytologist*.

Anderson R, Bayer PE, Edwards D. **2020**. Climate change and the need for agricultural adaptation. *Current Opinion in Plant Biology* **56**: 197–202.

Bertolino LT, Caine RS, Gray JE. **2019**. Impact of stomatal density and morphology on water-use efficiency in a changing world. *Frontiers in Plant Science* **10**.

Brocher J. **2015**. The BioVoxxel image processing and analysis toolbox. In: European BioImage Analysis Symposium.

Buckley TN. **2019**. How do stomata respond to water status? *New Phytologist*: 0–1.

Busch FA, Ainsworth EA, Amtmann A, Cavanagh AP, Driever SM, Ferguson JN, Kromdijk J, Lawson T, Leakey ADB, Matthews JSA, *et al.* 2024. A guide to photosynthetic gas exchange measurements: Fundamental principles, best practice and potential pitfalls. *Plant Cell and Environment*.

Deans RM, Brodribb TJ, Busch FA, Farquhar GD. **2019**. Plant water-use strategy mediates stomatal effects on the light induction of photosynthesis. *New Phytologist* **222**: 382–395.

Dittberner H, Korte A, Mettler-Altmann T, Weber APM, Monroe G, de Meaux J. **2018**. Natural variation in stomata size contributes to the local adaptation of water-use efficiency in Arabidopsis thaliana. *Molecular Ecology* **27**: 4052–4065.

Dore MHI. **2005**. Climate change and changes in global precipitation patterns: What do we know? *Environment International* **31**: 1167–1181.

Doyle W. **1962**. Operations useful for similarity-invariant pattern recognition. *Journal of the ACM (JACM)* **9**: 259–267.

Drake PL, Froend RH, Franks PJ. **2013**. Smaller, faster stomata: Scaling of stomatal size, rate of response, and stomatal conductance. *Journal of Experimental Botany* **64**: 495–505.

Durand M, Brendel O, Buré C, Le Thiec D. **2019**. Altered stomatal dynamics induced by changes in irradiance and vapour-pressure deficit under drought: impacts on the whole-plant transpiration efficiency of poplar genotypes. *New Phytologist* **222**: 1789–1802.

Duursma RA, Blackman CJ, Lopéz R, Martin-StPaul NK, Cochard H, Medlyn BE. **2019**. On the minimum leaf conductance: its role in models of plant water use, and ecological and environmental controls. *New Phytologist* **221**: 693–705.

Eyland D, van Wesemael J, Lawson T, Carpentier S. **2021**. The impact of slow stomatal kinetics on photosynthesis and water use efficiency under fluctuating light. *Plant Physiology* **186**: 998–1012.

Fanourakis D, Papadopoulou E, Valla A, Tzanakakis VA, Nektarios PA. **2021**. Partitioning of transpiration to cut flower organs and its mediating role on vase life response to dry handling: A case study in chrysanthemum. *Postharvest Biology and Technology* **181**: 111636.

Forster B, Van De Ville D, Berent J, Sage D, Unser M. **2004**. Complex wavelets for extended depth-of-field: A new method for the fusion of multichannel microscopy images. *Microscopy Research and Technique* **65**: 33–42.

Garcia A, Gaju O, Bowerman AF, Buck SA, Evans JR, Furbank RT, Gilliham M, Millar AH, Pogson BJ, Reynolds MP, *et al.* 2023. Enhancing crop yields through improvements in the efficiency of

696 photosynthesis and respiration. *New Phytologist* **237**: 60–77.

697 **Grantz DA, Zinsmeister D, Burkhardt J**. **2018**. Ambient aerosol
698 increases minimum leaf conductance and alters the aperture–flux
699 relationship as stomata respond to vapor pressure deficit (VPD).
700 *New Phytologist* **219**: 275–286.

701 **Haworth M, Marino G, Loreto F, Centritto M**. **2021**. Integrating
702 stomatal physiology and morphology: evolution of stomatal control
703 and development of future crops. *Oecologia* **197**: 867–883.

704 **Haworth M, Scutt CP, Douthe C, Marino G, Gomes MTG, Loreto F,**
705 **Flexas J, Centritto M**. **2018**. Allocation of the epidermis to stomata
706 relates to stomatal physiological control: Stomatal factors involved
707 in the evolutionary diversification of the angiosperms and
708 development of amphistomaty. *Environmental and Experimental*
709 *Botany* **151**: 55–63.

710 **Jones JJ, Huang S, Hedrich R, Geilfus CM, Roelfsema MRG**. **2022**.
711 The green light gap: a window of opportunity for optogenetic
712 control of stomatal movement. *New Phytologist* **236**: 1237–1244.

713 **Kaiser H**. **2009**. The relation between stomatal aperture and gas
714 exchange under consideration of pore geometry and diffusional
715 resistance in the mesophyll. *Plant, Cell and Environment* **32**: 1091–
716 1098.

717 **Kaiser H, Kappen L**. **1997**. In situ observations of stomatal
718 movements in different light-dark regimes: The influence of
719 endogenous rhythmicity and long-term adjustments. *Journal of*
720 *Experimental Botany* **48**: 1583–1589.

721 **Kaiser H, Kappen L**. **2000**. In situ observation of stomatal
722 movements and gas exchange of Aegopodium podagraria L. in the
723 understorey. *Journal of Experimental Botany* **51**: 1741–1749.

724 **Kaiser H, Kappen L**. **2001**. Stomatal oscillations at small apertures:
725 Indications for a fundamental insufficiency of stomatal feedback-
726 control inherent in the stomatal turgor mechanism. *Journal of*
727 *Experimental Botany* **52**: 1303–1313.

728 **Kaiser E, Morales A, Harbinson J**. **2018**. Fluctuating light takes crop
729 photosynthesis on a rollercoaster ride. *Plant Physiology* **176**: 977–
730 989.

731 **Kaiser H, Paoletti E**. **2014**. Dynamic stomatal changes. In: Tausz M,
732 Grulke N, eds. Plant Ecophysiology: Trees in a Changing
733 Environment. Springer Science+Business, 61–82.

734 **Kardiman R, Ræbild A**. **2018**. Relationship between stomatal
735 density, size and speed of opening in Sumatran rainforest species.
736 *Tree Physiology* **38**: 696–705.

737 **Lawson T, Blatt MR**. **2014**. Stomatal size, speed, and responsiveness
738 impact on photosynthesis and water use efficiency. *Plant Physiology*
739 **164**: 1556–1570.

Lawson T, Matthews J. **2020**. Guard Cell Metabolism and Stomatal Function. *Annual Review of Plant Biology* **71**: 273–302.

Lawson T, Vialet-Chabrand S. **2019**. Speedy stomata, photosynthesis and plant water use efficiency. *New Phytologist* **221**: 93–98.

Lehmann P, Or D. **2015**. Effects of stomata clustering on leaf gas exchange. *New Phytologist* **207**: 1015–1025.

Long SP, Taylor SH, Burgess SJ, Carmo-Silva E, Lawson T, De Souza AP, Leonelli L, Wang Y. **2022**. Into the Shadows and Back into Sunlight: Photosynthesis in Fluctuating Light. *Annual Review of Plant Biology* **73**: 617–648.

Lowe DG. **2004**. Distinctive image features from scale-invariant keypoints. *International journal of computer vision* **60**: 91–110.

Lthi BS, Thomas N, Hviid SF, Rueffer P. **2010**. An efficient autofocus algorithm for a visible microscope on a Mars lander. *Planetary and Space Science* **58**: 1258–1264.

Lundgren MR, Mathers A, Baillie AL, Dunn J, Wilson MJ, Hunt L, Pajor R, Fradera-Soler M, Rolfe S, Osborne CP, *et al.* 2019. Mesophyll porosity is modulated by the presence of functional stomata. *Nature Communications* **10**: 2825.

McAusland L, Vialet-Chabrand S, Davey P, Baker NR, Brendel O, Lawson T. **2016**. Effects of kinetics of light-induced stomatal responses on photosynthesis and water-use efficiency. *The New phytologist* **211**: 1209–1220.

Nadal M, Flexas J. **2019**. Variation in photosynthetic characteristics with growth form in a water-limited scenario: Implications for assimilation rates and water use efficiency in crops. *Agricultural Water Management* **216**: 457–472.

Novick KA, Ficklin DL, Stoy PC, Williams CA, Bohrer G, Oishi AC, Papuga SA, Blanken PD, Noormets A, Sulman BN, *et al.* 2016. The increasing importance of atmospheric demand for ecosystem water and carbon fluxes. *Nature Climate Change* **6**: 1023–1027.

Reza AM. **2004**. Realization of the contrast limited adaptive histogram equalization (CLAHE) for real-time image enhancement. *Journal of VLSI signal processing systems for signal, image and video technology* **38**: 35–44.

Sai N, Bockman JP, Chen H, Watson-Haigh N, Xu B, Feng X, Piechatzek A, Shen C, Gilliham M. **2023**. StomaAI: an efficient and user-friendly tool for measurement of stomatal pores and density using deep computer vision. *New Phytologist* **238**: 904–915.

Sakoda K, Yamori W, Groszmann M, Evans JR. **2021**. Stomatal, mesophyll conductance, and biochemical limitations to photosynthesis during induction. *Plant Physiology* **185**: 146–160.

De Souza AP, Wang Y, Orr DJ, Carmo-Silva E, Long SP. **2020**.

Photosynthesis across African cassava germplasm is limited by Rubisco and mesophyll conductance at steady state, but by stomatal conductance in fluctuating light. *New Phytologist* **225**: 2498–2512.

Taylor SH, Orr DJ, Carmo-Silva E, Long SP. **2020**. During photosynthetic induction, biochemical and stomatal limitations differ between Brassica crops. *Plant Cell and Environment* **43**: 2623–2636.

Vialet-Chabrand S, Dreyer E, Brendel O. **2013**. Performance of a new dynamic model for predicting diurnal time courses of stomatal conductance at the leaf level. *Plant, Cell and Environment* **36**: 1529–1546.

Xiong D, Douthe C, Flexas J. **2018**. Differential coordination of stomatal conductance, mesophyll conductance, and leaf hydraulic conductance in response to changing light across species. *Plant Cell and Environment* **41**: 436–450.

Xiong Z, Xiong D, Cai D, Wang W, Cui K, Peng S, Huang J. **2022**. Effect of stomatal morphology on leaf photosynthetic induction under fluctuating light across diploid and tetraploid rice. *Environmental and Experimental Botany* **194**: 104757.

Zhang N, Berman SR, Joubert D, Vialet-Chabrand S, Marcelis LFM, Kaiser E. **2022**. Variation of Photosynthetic Induction in Major Horticultural Crops Is Mostly Driven by Differences in Stomatal Traits. *Frontiers in Plant Science* **13**: 1–19.

Supporting Information

SM Fig 1. Example of stomatal aperture dynamics of a single stoma and the model fit for opening (t=30-90) and closing (t=90-120). Raw aperture data is in black and the model fit curve in red.

SM Fig. 2 Stomatal aperture dynamics of focus projection images (automatic) and manually determined best single focus images (manual) demonstrating their correlation.

SM Fig. 3 Example of how the position of the best focus for a stoma can change in a stack during the shade-sun-shade experiment due to the movement of the leaf surface (Fig. 5).

SM Movie 1 Example of a processed z-stack (100images) of a single timepoint in the experiment. Stomata positions are indicated by red ovals.

SM movie 2 Example of the processed time stack (video) of a full experiment (119 focus projections of the z-stacks of each timepoint). Stomata positions are indicated by red ovals.

SM video 3 Example of the processed time stack (video) of a full experiment, zoomed in on a single stoma.

SM video 4 The same video of 3 after thresholding.

SM video 5 The same video as 3 and 4 after segmentation.